Circular Dichroism and Magnetic Circular Dichroism Studies of the Reduced Binuclear Non-Heme Iron Site of Stearoyl-ACP Δ^9-Desaturase: Substrate Binding and Comparison to Ribonucleotide Reductase

Yi-Shan Yang,[†] John A. Broadwater,[‡] Sabine Coates Pulver,[†] Brian G. Fox,*,[‡] and Edward I. Solomon*,[†]

Contribution from The Department of Chemistry, Stanford University, Stanford, California 94305, and The Institute for Enzyme Research, Graduate School and Department of Biochemistry, College of Agricultural and Life Sciences, University of Wisconsin, Madison, Wisconsin 53705

Received June 29, 1998

Abstract: Stearoyl-acyl carrier protein (stearoyl-ACP) Δ^9-desaturase (Δ^9D) catalyzes the insertion of a cis double bond between the 9 and 10 positions of the stearoyl-ACP to convert it to oleoyl-ACP. The binuclear non-heme iron active site of the fully reduced enzyme (reduced Δ^9D) and its substrate-bound form (stearoyl-ACP Δ^9D) have been studied using a combination of circular dichroism (CD) and magnetic circular dichroism (MCD) to probe their geometric and electronic structures. CD and MCD in the near-IR region probe the ligand-field d−d transitions of the ferrous sites. Variable-temperature variable-field (VTVH) MCD combined with a spin-Hamiltonian analysis including the zero-field splitting (ZFS) of both irons and the exchange coupling (J) between the irons due to bridging ligation is used to probe their ground-state properties. These ground- and excited-state results indicate that the active site of reduced Δ^9D has two equivalent 5-coordinate irons in a distorted square pyramidal geometry. They are weakly antiferromagnetically coupled with large negative and equivalent ZFSs ($D_1 = D_2 < 0$), which gives a diamagnetic ground state interacting with low-lying paramagnetic excited states. Addition of substrate causes a significant change in both the excited states and the nature of the ground state. These spectral changes indicate that one of the irons becomes 4-coordinate, while the other distorts toward a trigonal bipyramidal geometry. The two irons remain weakly antiferromagnetically coupled. However, this geometry change modifies their ZFSs ($D_1 < 0$ and $D_2 > 0$), which results in a new ground state, $M_s = \pm 1$, with a low-lying $M_s = \pm 2$ first excited state. These results are the first direct evidence that the stearoyl-ACP binding strongly perturbs the active site, creating an additional open coordination position that correlates with enhanced dioxygen reactivity. These results are correlated with the X-ray crystal structure and compared to the related enzyme, ribonucleotide reductase, to gain insight into geometric and electronic structure contributions to dioxygen reactivity.

Introduction

Binuclear non-heme iron active sites have been found in a number of metalloenzymes and proteins performing a variety of biological functions.[1−3] Members of this class include hemerythrin (Hr),[4−6] methane monooxygenase (MMO),[2,7,8] toluene-4-monooxygenase (T4MO),[9] alkane ω-hydroxylase (AlkB),[10] ribonucleotide reductase (RR),[3,11−15] the acyl-acyl carrier protein (acyl-ACP) desaturases,[16,17] the purple acid phosphatases (PAPs),[18,19] rubrerythrin (Rb),[20,21] and nigerythrin.[22] They all have magnetic coupling between the irons

[†] Stanford University.

[‡] University of Wisconsin.

(1) Fox, B. G. Catalysis by Non-Heme Iron-Containing Enzymes. In *Comprehensive Biological Catalysis*; Sinnott, M., Ed.; Academic Press: London, 1997; Vol. 3, pp 261−348.

(2) Wallar, B.; Lipscomb, J. D. *Chem. Rev.* **1996**, *96*, 2625−2657.

(3) Feig, A. L.; Lippard, S. J. *Chem. Rev.* **1994**, *94*, 759−805.

(4) Stenkamp, R. E. *Chem. Rev.* **1994**, *94*, 715−726.

(5) Holmes, M. A.; Trong, I. L.; Turley, S.; Sieker, L. C.; Stenkamp, R. E. *J. Biol. Chem.* **1991**, *218*, 583−593.

(6) Holmes, M. A.; Stenkamp, R. E. *J. Biol. Chem.* **1991**, *220*, 723−737.

(7) Rosenzweig, A. C.; Frederick, C. A.; Lippard, S. J.; Nordlund, P. *Nature* **1993**, *366*, 537−543.

(8) Rosenzweig, A. C.; Nordlund, P.; Takahara, P. M.; Frederick, C. A.; Lippard, S. J. *Chem. Biol.* **1995**, *2*, 409−418.

(9) Pikus, J. D.; Studts, J. M.; Achim, C.; Kauffmann, K. E.; Münck, E.; Steffan, R. J.; McClay, K.; Fox, B. G. *Biochemistry* **1996**, *35*, 9106−9119.

(10) Shanklin, J.; Achim, C.; Schmidt, H.; Fox, B. G.; Münck, E. *Proc. Natl. Acad. Sci. U.S.A.* **1997**, *94*, 2981−2986.

(11) Ravi, N.; Bollinger, J. M. Jr.; Huynh, B. H.; Edmondson, D. E.; Stubbe, J. *J. Am. Chem. Soc.* **1994**, *116*, 8007−8014.

(12) Bollinger, J. M. Jr.; Tong, W. H.; Ravi, N.; Huynh, B. H.; Edmondson, D. E.; Stubbe, J. *J. Am. Chem. Soc.* **1994**, *116*, 8015−8023.

(13) Bollinger, J. M. Jr.; Tong, W. H.; Ravi, N.; Huynh, B. H.; Edmondson, D. E.; Stubbe, J. *J. Am. Chem. Soc.* **1994**, *116*, 8024−8032.

(14) Nordlund, P.; Eklund, H. *J. Biol. Chem.* **1993**, *232*, 123−164.

(15) Logan, D. T.; Su, X.-D.; Åberg, A.; Regnström, K.; Hajdu, J.; Eklund, H.; Nordlund, P. *Structure* **1996**, *4*, 1053−1064.

(16) Shanklin, J.; Cahoon, E. B. *Annu. Rev. Plant Physiol. Plant Mol. Biol.* **1998**, *49*, 611−641.

(17) Lindqvist, Y.; Huang, W.; Schneider, G.; Shanklin, J. *EMBO J.* **1996**, *15*, 4081−4092.

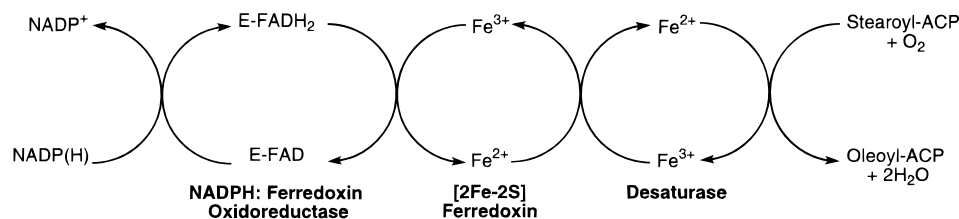(18) Klabunde, T.; Krebs, B. *Struct. Bonding* **1997**, *89*, 177−198.

(19) Klabunde, T.; Sträter, N.; Fröhlich, R.; Witzel, H.; Krebs, B. *J. Biol. Chem.* **1996**, *259*, 737−748.

(20) Bonomi, F.; Kurtz, D. M. Jr.; Cui, X. *J. Biol. Inorg. Chem.* **1996**, *1*, 67−72.

(21) deMaré, F.; Kurtz, D. M. Jr.; Nordlund, P. *Nat. Struct. Biol.* **1996**, *3*, 539−546.

(22) Pierik, A. J.; Wolbert, R. B. G.; Portier, G. L.; Verhagen, M. F. J. M.; Hagen, W. R. *Eur. J. Biochem.* **1993**, *212*, 237−245.

Scheme 1

associated with the presence of bridging ligands and are often involved in reactions with dioxygen. Hr reversibly binds dioxygen for transport and storage. MMO, T4MO, and AlkB activate dioxygen for the hydroxylation of methane, toluene, and the methyl group of an alkane to produce their corresponding alcohols. RR reacts with dioxygen and generates a tyrosyl radical necessary for the reduction of ribonucleotides to deoxyribonucleotides. The acyl-ACP desaturases activate dioxygen for the insertion of a cis double bond. PAPs catalyze the hydrolysis of phosphate esters, and Rb and nigerythrin are considered to have ferroxidase functions. Among these enzymes, RR, MMO, T4MO, AlkB, and the acyl-ACP desaturases are involved in reactions with dioxygen and are considered to share similar aspects of their catalytic cycles.[9,10,23-26]

Desaturation is an essential step in fatty acid biosynthesis. In eukaryotes, desaturation is a postsynthetic modification that is catalyzed by NADPH- and dioxygen-dependent non-heme binuclear iron enzymes. Both membrane-bound and soluble (found only in plants and cyanobacteria) enzymes have been identified, and a large variety of isoforms that vary in substrate specificity and regiospecificity are known within these genetically and structurally distinct homologues.[16,27,28] Free fatty acids are not desaturated in vivo, but are rather attached by a phosphopantetheine thioester linkage to acyl carrier protein (ACP) for the soluble desaturases,[29] to coenzyme A for some membrane-bound desaturases,[27,28] or to sugar or phospholipid moieties for other membrane-bound forms.[27,28]

Stearoyl-acyl carrier protein Δ⁹-desaturase (Δ⁹D) from castor seeds is the best characterized soluble desaturase. This enzyme inserts the cis double bond between the 9 and 10 positions of stearoyl-ACP to form oleoyl-ACP using the electron-transfer chain shown in Scheme 1.[30-33] Δ⁹D is a homodimer with each subunit having one binuclear iron site and a molecular weight of 40 000 .[34] Both the met [Fe(III)Fe(III)] (oxidized) and the fully reduced [Fe(II)Fe(II)] (diferrous) forms have been char-
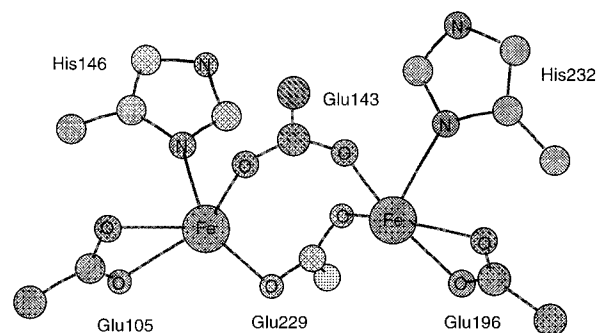

Figure 1. Representation of the crystallographically determined (ref 17) binuclear Fe(II)Fe(II) active site of stearoyl-acyl carrier protein Δ⁹-desaturase from castor seed.

acterized. UV−vis spectroscopy[35] of the oxidized form reveals the presence of ligand to metal charge-transfer transitions between 300 and 700 nm that are consistent with the presence of the μ-oxo bridge between the two Fe(III) atoms as observed in other oxo-bridged enzymes, i.e., metHr,[36,37] metRR,[38,39] and metRr.[40] From resonance Raman spectroscopy, symmetric and asymmetric vibrational modes are observed at $\nu_s = 519$ cm^{-1} and $\nu_{as} = 747$ cm^{-1}, which are typical Fe−O−Fe vibration modes.[35] In H$_2$^{18}O, these frequencies shift by −18 and −34 cm^{-1}, respectively, indicating that the bridging ligand is exchangeable with solvent.[35] Mössbauer studies have been pursued for both the diferric and reduced forms.[41] The two Fe-(III) atoms in the oxidized form are strongly antiferromagnetically coupled with $-J > 30$ cm^{-1} ($H = -2JS_1S_2$), providing further evidence of the existence of μ-oxo ligation, while the reduced form has quadrupole splitting and isomer shift parameters typical of high-spin Fe(II) in a 5- or 6-coordinate environment of nitrogen or oxygen ligands.

The three-dimensional structure of reduced Δ⁹D from castor seeds has been determined to a resolution of 2.4 Å.[17] The active site structure (Figure 1) shows that the two Fe(II) atoms are bound in a highly symmetric environment: one iron is coordinated by Glu196 and His232, while the other iron is coordinated by Glu105 and His146, with both Glu196 and Glu105 binding in a bidentate mode. The two irons are μ-1,3-bridged by two carboxylate ligands (Glu229 and Glu143). The long distance between the irons (4.2 Å) indicates that a μ-O(H) bridge is not present, which is consistent with the lack of electron density observed in this region of the structure.

(23) Kurtz, D. M. Jr. *J. Biol. Inorg. Chem.* **1997**, *2*, 159−167.

(24) Que, L. Jr.; Dong, T.; Shu, L.; Wilkinson, E. C. In *Spectroscopic Methods in Bioinorganic Chemistry*; Solomon, E. I., Hodgson, K. O., Eds.; ACS Symposium Series; American Chemical Society: Washington, DC, 1998; Vol. 692, pp 374−386.

(25) Bollinger, J. M., Jr.; Krebs, C.; Vicol, A.; Chen, S.; Ley, B. A.; Edmondson, D. E.; Huynh, B. H. *J. Am. Chem. Soc.* **1998**, *120*, 1094−1095.

(26) Bollinger, J. M. Jr.; Edmondson, D. E.; Huynh, B. H.; Filley, J.; Norton, J. R.; Stubbe, J. *Science* **1991**, *253*, 292−298.

(27) Gunstone, F. D. In *Fatty Acid and Lipid Chemistry*, 1st ed.; Blackie Academic & Professional: London, 1996.

(28) *Fatty Acid Metabolism and Its Regulation*; Numa, S., Ed.; Elsevier Science Publishers B. V.: New York, 1984.

(29) Nagai, J.; Bloch, K. *J. Biol. Chem.* **1966**, *241*, 1925−1927.

(30) Holloway, P. W. In *The Enzymes*, 3rd ed.; Boyer, P. D., Ed.; Academic: New York, 1983; pp 63−83.

(31) Nagai, J.; Bloch, K. *J. Biol. Chem.* **1996**, *243*, 4626−4633.

(32) Schmidt, H.; Heinz, E. *Plant Physiol.* **1990**, *94*, 214−220.

(33) Wada, H.; Schmidt, H.; Heinz, E.; Murata, N. *J. Bacteriol.* **1993**, *175*, 544−547.

(34) Shanklin, J.; Somerville, C. *Proc. Natl. Acad. Sci. U.S.A.* **1991**, *88*, 2510−2514.

(35) Fox, B. G.; Shanklin, J.; Ai, J.; Loehr, T. M.; Sanders-Loehr, J. *Biochemistry* **1994**, *33*, 12776−12786.

(36) Schiemke, A. K.; Loehr, T. M.; Sanders-Loehr, J. *J. Am. Chem. Soc.* **1986**, *108*, 2437−2443.

(37) Gay, R. R.; Solomon, E. I. *J. Am. Chem. Soc.* **1978**, *100*, 1972.

(38) Sjöberg, B.-M.; Loehr, T. M.; Sanders-Loehr, J. *Biochemistry* **1982**, *21*, 96−102.

(39) Ling, J.; Sahlin, M.; Sjöberg, B. M.; Loehr, T. M.; Sanders-Loehr, J. *J. Biol. Chem.* **1994**, *269*, 5595−5601.

(40) Dave, B. C.; Czernuszewicz, R. S.; Prickril, B. C.; Kurtz, D. M., Jr. *Biochemistry* **1994**, *33*, 3572−3576.

(41) Fox, B. G.; Shanklin, J.; Somerville, C.; Münck, E. *Proc. Natl. Acad. Sci. U.S.A.* **1993**, *90*, 2486-2490.

MMO, RR, and Δ^9D share substantial similarities in their amino acid sequences and the physical properties of their binuclear active sites.[17] Thus, these enzymes likely have common features in their catalytic cycles, including the generation of a diferrous state, Fe(III)-peroxo, and high-valent Fe-(IV)-oxo intermediates. However, the functional diversity of this group (desaturation, hydroxylation, radical formation) necessitates divergence of mechanism at some point in catalysis. One clear difference between the enzymes has been observed in the oxidation of the diferrous enzymes. The diferrous center of RR is oxidized by dioxygen in the absence ($\sim$10 min^{-1}) or presence ($\sim$60 min^{-1}) of the active site Tyr residue with comparable rates.[42] Similarly, the addition of methane stimulates the oxidation of diferrous MMO only modestly (from $\sim$1 to $\sim$10 min^{-1}).[2] In contrast, the Δ^9D diferrous center is oxidized extremely slowly by dioxygen ($\sim$0.001 min^{-1}) in the absence of substrate, but is capable of steady-state turnover rates of $\sim$30 min^{-1}.[43,44] The electronic and structural differences contributing to this diverse range of reactivities is the focus of the present study.

Non-heme ferrous sites have been difficult to study as they are not easily accessible through the usual spectroscopic methods such as EPR and electronic absorption. However, a combination of circular dichroism (CD), magnetic circular dichroism (MCD), and variable-temperature variable-field (VTVH) MCD in the near-IR region provides a direct probe of the excited and ground states of the non-heme ferrous sites.[45,46] CD and MCD allow the observation of ligand-field electronic transitions that are very weak in absorption while ground-state information including exchange coupling and zero-field splitting (ZFS) can be obtained through analysis of VTVH MCD saturation magnetization data. High-spin d^6 Fe(II) in an octahedral ligand field has a $^5T_{2g}$ ground state and an ^5E_g excited state split by $\sim$10 000 cm^{-1} ($10Dq$) for biologically relevant nitrogen and oxygen ligands. The low symmetry of a protein site removes the degeneracy of the ^5E_g excited state, resulting in a pair of transitions split by up to $\sim$2000 cm^{-1}. Removal of one of the axial ligands typically leads to the formation of a square pyramidal 5-coordinate structure. This large axial perturbation results in the energy splitting of the two components of the ^5E_g being on the order of 5000 cm^{-1}. Distortion of a square pyramidal geometry into a trigonal bipyramidal structure decreases the transition energy of the two ^5E_g components (highest energy component at <10 000 cm^{-1}). For tetrahedral ferrous coordination, $10Dq_{Td}$ is equal to $-(4/9)10Dq_{Oh}$, resulting in the highest energy ligand-field transitions in the region of $\sim$5000 to $\sim$7000 cm^{-1}.

In this study, the [Fe(II)Fe(II)] centers in reduced Δ^9D and its substrate-bound form (stearoyl-ACP Δ^9D) are investigated using a combination of excited spectral methods (CD and MCD). Their dimer ground-state magnetic properties are determined via a spin-Hamiltonian analysis of the VTVH MCD data. Together, these data provide a direct probe of geometric and electronic structure and the interaction between the irons in the active sites of both species. The results obtained are compared with the crystal structure, used to investigate the substrate perturbation on the active site and its relation to increased

dioxygen reactivity. By comparison to our prior results on RR and MMO, we provide insight into the similarities and differences in geometric and electronic structure that can contribute to the catalytic mechanism and trends in dioxygen reactivity of the binuclear non-heme iron enzymes.

Experimental Section

Δ^9D was expressed, purified, and characterized as previously described.[47] Spinach ACP isoform I was produced by coexpressing a synthesized spinach ACP gene with the gene for *E. coli* holo-ACP synthase.[48] Holo-ACP was converted to stearoyl-ACP (>95%) using partially purified preparations of recombinant *E. coli* acyl-ACP synthase containing a C-terminal His6 tag.[49] Denaturing gel electrophoresis and electrospray ionization mass spectrometry were used to characterize the extent of phophopantetheinylation, acylation, and removal of the N-terminal methionine in the apo-, holo-, and stearoyl-ACP preparations. The concentration of desaturase protein was determined by its extinction coefficient (molar absorptivity of 4200 M^{-1} cm^{-1} per diiron center, or 8400 M^{-1} cm^{-1} per desaturase dimer) and by the Bradford dye binding assay.[41] Holo-ACP and stearoyl-ACP were quantitated by reaction of Ellman's reagent with the phosphopantetheine thiol group of either holo-ACP or holo-ACP formed by treating the stearoyl-ACP with NH$_2$OH. Further details of the ACP-production process will be reported elsewhere.[50]

Purified protein (either desaturase or spinach stearoyl-ACP) was concentrated to $\sim$2 mM per diiron center by ultrafiltration (Amicon stirred ultrafiltration cell, Beverly, MA) using YM3 (ACP) or YM30 (Δ^9D) membranes. This process was repeated until the percentage of D$_2$O was greater than 99.9% of the solvent and the protein concentration was $\sim$3 mM (Δ^9D) or $\sim$6 mM (ACP). Next, 85% d_3-glycerol (made in 0.4 M Hepes, 50 mM NaCl, pD 7.6) was added to obtain a solution of $\sim$50% d_3-glycerol, with 1.6 mM Δ^9D (3.2 mM diiron centers) or 6 mM stearoyl-ACP. The desaturase was reduced to the diferrous state with repeated cycles of evacuation and argon flushing followed by chemical reduction with methyl viologen (50 mM) and excess sodium dithionite. Stearoyl-ACP was made anaerobic with repeated cycles of evacuation and argon flushing. The amount of methyl viologen added was controlled to be less than $\sim$1.5 mM to avoid the presence of a detectable signal in the MCD spectrum at $\sim$12 000 cm^{-1}.

Circular dichroism studies were performed on a JASCO J-200D spectropolarimeter operating with a liquid nitrogen-cooled InSb detector in the 600–2000 nm region. Low-temperature magnetic circular dichroism data were acquired on this spectropolarimeter, modified to accommodate an Oxford Instruments SM4000-7T superconducting magnet capable of magnetic fields up to 7.0 T and temperatures down to 1.6 K.

Protein samples prepared for MCD studies were slowly inserted into the cryostat to reduce strain in the resulting optical glass. The depolarization of the protein glass was checked by measuring the CD spectrum of a freshly prepared nickel (+)-tartrate solution placed immediately before and after the MCD sample. Typically less than $\sim$5% of depolarization was observed.

The baseline-corrected CD and MCD spectra were fit to Gaussian band shapes using a constrained nonlinear least-squares fitting procedure. Each spectroscopic method has different selection rules; thus, transitions can have different intensities and signs, but the energies are similar. The MCD spectra are taken at low temperature; thus, they may have significantly sharper bandwidths, and the band energies may shift by a limited amount relative to the room-temperature CD data, which were allowed to float in the final fit. VTVH MCD data (MCD intensity, temperature, and applied magnetic field) were fit using a simplex routine that minimizes the χ^2 value. A goodness of fit parameter (χ^2/number of float parameters) was utilized in the comparison of different fit results.

(42) Tong, W. H.; Chen, S.; Lloyd, S. G.; Edmondson, D. E.; Huynh, B.-H.; Stubbe, J. *J. Am. Chem. Soc.* **1996**, *118*, 2107–2108.

(43) Broadwater, J. A.; Ai, J.; Loehr, T. M.; Sanders-Loehr, J. Fox, B. G. *Biochemistry* **1998**, *37*, 14664–14671.

(44) Cahoon, E. B.; Lindqvist, Y.; Schneider, G.; Shanklin, J. *Proc. Natl. Acad. Sci. U.S.A.* **1997**, *94*, 4872–4877.

(45) Pulver, S.; Froland, W. A.; Fox, B. G.; Lipscomb, J. D.; Solomon, E. I. *J. Am. Chem. Soc.* **1993**, *115*, 12409–12422.

(46) Reem, R. C.; Solomon, E. I. *J. Am. Chem. Soc.* **1987**, *109*, 1216–1226.

(47) Hoffman, B. J.; Broadwater, J. A.; Johnson, P. A.; Harper, J.; Fox, B. G.; Kenealy, W. R. *Protein Express. Purif.* **1995**, *6*, 646–654.

(48) Lambolot, R. H.; Walsh, C. T. *J. Biol. Chem.* **1995**, *270*, 24658–24661.

(49) Rock, C. O.; Garwin, J. L. *J. Biol. Chem.* **1979**, *254*, 7123–7128.

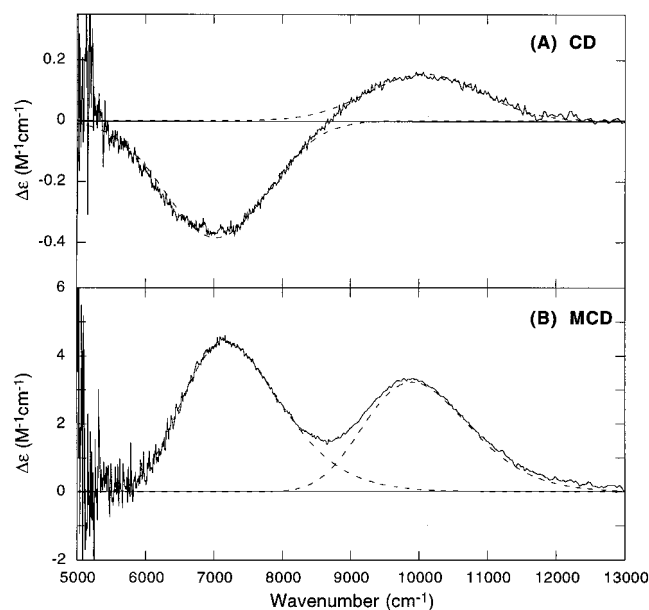(50) Broadwater, J. A.; Fox, B. G. Manuscript in preparation.

Non-Heme Iron Site of Stearoyl-ACP Δ^9D

J. Am. Chem. Soc., Vol. 121, No. 12, 1999 2773

Figure 2. (A) CD and (B) LT MCD spectra of the binuclear non-heme Fe(II)Fe(II) active site in reduced Δ^9-desaturase. The experimental data (—) are fit to individual Gaussian band shapes (- - -). The CD and low-temperature MCD spectra were recorded at 5 °C and 5 K, 7 T, respectively.

Table 1. Summary of CD and MCD Gaussian Resolution Analysis Results for Reduced Binuclear Non-Heme Δ^9-Desaturase (Reduced Δ^9D) and Substrate-Bound Δ^9-Desaturase (Stearoyl-ACP Δ^9D) in the Ligand-Field Region

band		reduced Δ^9D		stearoyl-ACP Δ^9D	
		CD	MCD	CD	MCD
1	energy (cm^{-1})	7030 (−)	7160 (+)	5000 (−)	5535 (+)
	HWHM (cm^{-1})	880	760	1480	750
2	energy (cm^{-1})	10080 (+)	9920 (+)	7890 (−)	
	HWHM (cm^{-1})	960	870	810	
3	energy (cm^{-1})			9650 (+)	9156 (−)
	HWHM (cm^{-1})			1130	800

Results and Analysis

A. Excited States. Figure 2 gives room-temperature CD and low-temperature MCD spectra of reduced Δ^9D in the near-IR region (from 13 000 to 5000 cm^{-1}). One negative peak and one positive peak are observed in the CD spectrum, whereas two positive peaks are observed in the MCD spectrum. Neither addition of glycerol nor pH change (pH 6.0−8.5) affects the spectra. The dashed lines in Figure 2 give the simultaneous Gaussian resolution with parameters summarized in Table 1. Two transitions at 7100 ± 60 and 10 000 ± 80 cm^{-1} are required to fit both spectra. The presence of only two transitions in the 5500−12000 cm^{-1} region indicates that both irons are approximately equivalent, and are either 6-coordinate or 5-coordinate. We rule out the possibility that the irons are 6-coordinate on the basis of ligand-field calculations[45,46] and model studies[51] that have shown the lowest band energy for 6-coordinate model complexes is at >~8000 cm^{-1}. Since the highest energy band is at ~10 000 cm^{-1}, these irons are 5-coordinate square pyramidal. However, the relatively small energy splitting of these two transitions (~2900 cm^{-1}) suggests that both irons have an unusually distorted square pyramidal geometry (vide infra).
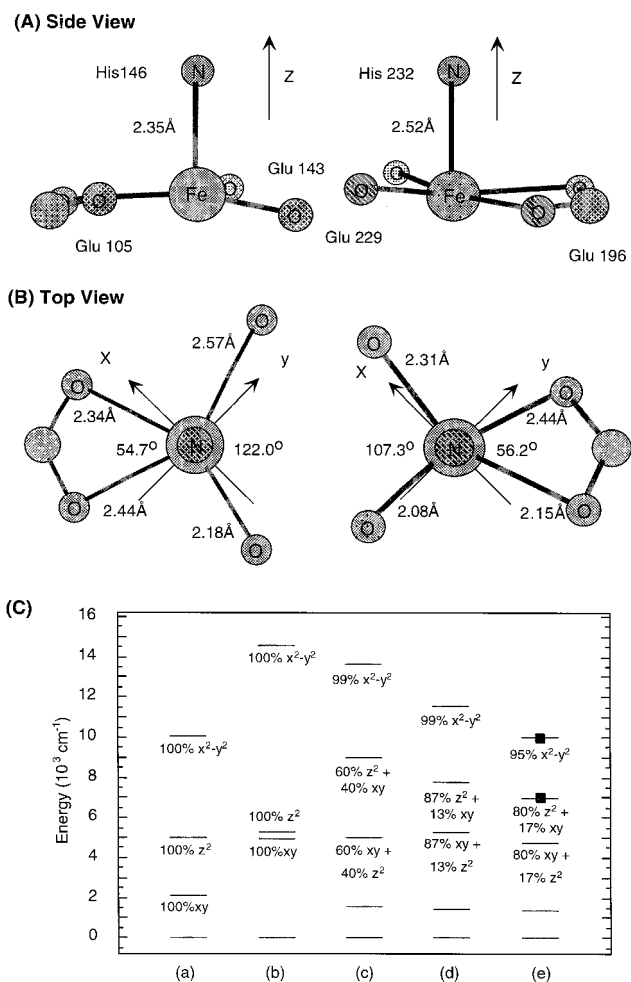
(51) Pavel, E. G.; Kitajima, N.; Solomon, E. I. *J. Am. Chem. Soc.* **1998**, *120*, 3949−3962.

(52) Companion, A. L.; Komarynsky, M. A. *J. Chem. Educ.* **1964**, *41*, 257−262.

Figure 3. (A) Side view and (B) top view for the orientation of the two Fe(II) sites in reduced Δ^9-desaturase. The coordinate system obtained from the ligand-field calculation is indicated. (C) d-orbital energy level diagrams resulting from ligand-field calculations of a series of models with (a) an ideal 5-coordinate square pyramidal geometry, (b) an effect of elongated z-axis, (c) an effect of two-in−two-out geometry, (d) an effect of asymmetric bond lengths, and (e) reduced Δ^9-desaturase. Calculated energies (—) are compared to experiment (■). Wave function descriptions use the axis orientation indicated in (A) and (B).

To gain insight into the electronic structure of each iron in the active site, the method of Campanion and Komarynsky was utilized to calculate the ligand-field (LF) energy levels and wave functions.[52] A LF model of the reduced Δ^9D active site was constructed on the basis of the coordinates from the crystal structure. As shown in Figure 3A,B, for both irons, the N_{His}−Fe bonds are chosen to be the z-axis, the x-axis is rotated 45° from the bisector of the two O_{Glu}−Fe bonds of the terminal bidentate glutamic acid residues (Glu196 and Glu105), and the y-axis is perpendicular to the x- and z-axes. A number of structural features should be noticed: both iron sites have (1) a long axial bond length of N_{His}−Fe (2.35 and 2.52 Å, side view, Figure 3A), (2) an extremely small O_{Glu}−Fe−O_{Glu} angle for the bidentate glutamic acid residue (54.7° and 56.2°) and an associated large O_{Glu}−Fe−O_{Glu} angle of the two bridging glutamic acid residues (122.0° and 107.3°), which generates a highly distorted ligand field in the xy-plane ("two-in−two-out" geometry, top view, Figure 3B), and (3) asymmetric Fe−O bond distances for the bidentate carboxylates and between the two bridging glutamic acid residues. Initial estimates of the LF parameters, α_2 and α_4, of each ligand were based on model

complexes but were allowed to vary systematically according to their relative strength based on the type of ligands (N or O) and their bond lengths.[53-56]

Figure 3C gives a series of calculated energy level diagrams. The calculation was first performed on a model with an ideal 5-coordinate square pyramidal (5C SP) geometry with one axial N and four equatorial O atoms (Figure 3C(a)). The structural features were then introduced, including a long *z*-axis (Figure 3C(b)), a distorted *xy*-plane (two-in−two-out geometry, vide supra, Figure 3C(c)), and asymmetric bond lengths of the adjacent Fe−O bonds (Figure 3C(d)). The coordinates and parameters were refined to be consistent with the crystal structure of reduced Δ^9D and the CD/MCD spectral data (Figure 3C(e)). The ideal 5C SP presents three transitions to d_{xy}, d_{z^2}, and $d_{x^2-y^2}$ at ∼2000, 5000 and 10 000 cm^{-1}, respectively (3C-(a)), which is consistent with the ligand-field theory with Δ^5E_g = ∼5000 cm^{-1} (vide supra). Elongation of the *z*-axis further increases Δ^5E_g (Figure 3C(b)). The two-in−two-out geometry shows a large perturbation on the energy level diagram (Figure 3C(c)). This distortion not only significantly decreases the energy of $d_{x^2-y^2}$, but also increases the energy of d_{xy}, which undergoes a configuration interaction with the d_{z^2} orbital and increases the d_{z^2} energy. Thus, these two orbitals mix and the Δ^5E_g is decreased to ∼4000 cm^{-1}. Allowing the adjacent Fe−O bonds to be asymmetric further decreases the energy difference between these transitions, and the mixing of d_{xy} and d_{z^2} (Figure 3C(d)). Finally, refining the coordinates and parameters to be consistent with the crystal structure of the reduced Δ^9D gives the high-energy ligand-field d−d transitions at ∼7000 and 10 000 cm^{-1} (Figure 3C(e)), which reproduces the CD/MCD results in Figure 2. Note that the d_{z^2} transition is predicted at ∼4700 cm^{-1} while it is not observed in the CD/MCD spectra. This indicates that the LF model overestimates the T_{2g} splitting as it does not describe π bonding interactions.

In conclusion, the combined effects of the two-in−two-out geometry and asymmetric bonding distances in the *xy*-plane (Figure 3B) significantly perturb the ligand field of the reduced Δ^9D. It causes an unusually small energy splitting between the high-energy d−d transitions, ∼3000 cm^{-1}, which is consistent with a square pyramidal geometry highly distorted in the *xy*-plane. The LF calculation also indicates that both transitions are *x*,*y*-polarized and the zero-field splitting on both irons should be negative, which are consistent with the results obtained from the ground-state analysis (vide infra). Thus, the CD/MCD data indicate that the two irons in the active site of reduced Δ^9D have approximately equivalent, 5-coordinate centers with an extremely distorted square pyramidal geometry. This assignment is consistent with the coordination environment determined in the reduced crystal structure, and emphasizes the similarity of the biferrous ligation environment in both solution and the crystalline state. Moreover, it is noteworthy that the same ligation environment was achieved by either chemical reduction (solution state) or photoreduction (crystals).[17]

The addition of apo-ACP (lacking the functionally essential phosphopantetheine group) or holo-ACP (lacking the stearoyl chain attached to the phosphopantethiene sulfhydryl group) elicited no change in either CD or MCD spectral properties as compared to reduced Δ^9D alone. However, the near-IR CD
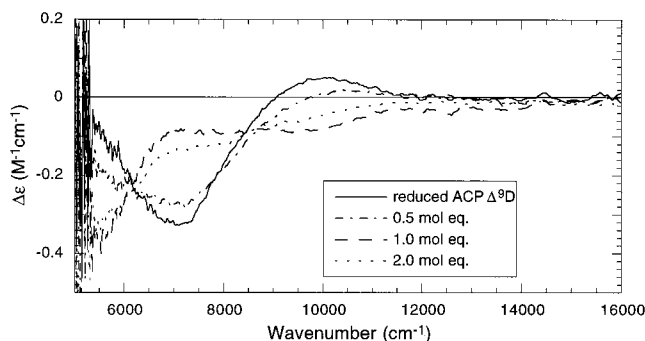

Figure 4. CD spectra recorded at 5 °C of reduced Δ^9-desaturase in the presence of a 0 (—), 0.5 (− − −), 1.0 (-·-), and 2.0 (···) molar equivalence of substrate (stearoyl-ACP).
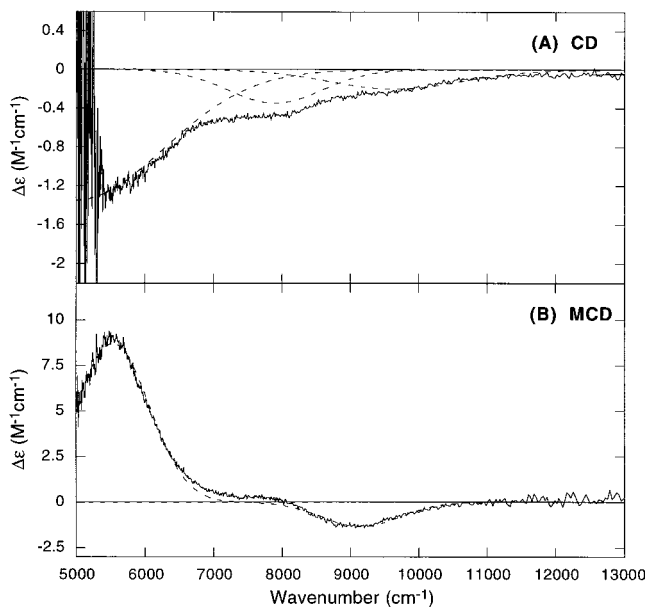

Figure 5. (A) CD and (B) LT MCD spectra of the binuclear non-heme Fe(II)Fe(II) active site in stearoyl-ACP Δ^9-desaturase. The experimental data (—) were fit to individual Gaussian band shapes (- - -). The CD and low-temperature MCD spectra were recorded at 5 °C and 5 K, 7 T, respectively.

spectrum of reduced Δ^9D shows a dramatic change upon the addition of substrate (18:0-stearoyl-ACP).

Figure 4 presents the CD spectra of the reduced form in the presence of 0.5-, 1.0-, and 2.0-fold molar equivalents of substrate. Further addition of substrate produces no significant change. Figure 4 shows that titration of substrate completely alters the CD spectrum of the reduced form. The new transitions are now observed at ∼5000, ∼8000 and ∼9500 cm^{-1}. The binding constant is estimated[57] to be K_b = 1200 ± 400 M^{-1}.

Figure 5 compares the room-temperature CD and low-temperature MCD spectra of stearoyl-ACP Δ^9D in the near-IR region (from 13 000 to 5000 cm^{-1}) corresponding to the three new peaks observed at ∼9600, ∼7900, and ∼5000 cm^{-1} in the CD spectrum. The MCD spectrum shows one negative peak at ∼9200 cm^{-1}, one positive peak at ∼5500 cm^{-1}, and a positive shoulder at ∼7500 cm^{-1}. The dashed lines in Figure 5 give the simultaneous Gaussian resolution, in which a minimum of three bands are required to fit both the CD and MCD spectra with the parameters summarized in Table 1. These CD/MCD spectral changes indicate that, upon substrate binding, both irons in reduced Δ^9D are significantly perturbed and no longer equiva-

(53) Long, G. L.; Clarke, P. J. *Inorg. Chem.* **1978**, *17*, 1394−1401.
(54) Miller, L. L.; Jacobson, R. A.; Chen, Y.-S.; Kurtz, D. M. *Acta Crystallogr.* **1989**, *C45*, 527−529.
(55) Vaira, D. M.; Orioli, P. L. *Acta Crystallogr.* **1968**, *B24*, 1269−1272.
(56) Montgomery, H.; Chastain, R. V.; Natt, J. J.; Witkowska, A. M.; Lingafelter, E. C. *Acta Crystallogr.* **1967**, *22*, 775−780.
(57) Rose, N. J.; Drago, R. S. *J. Am. Chem. Soc.* **1959**, *81*, 6138−6141.
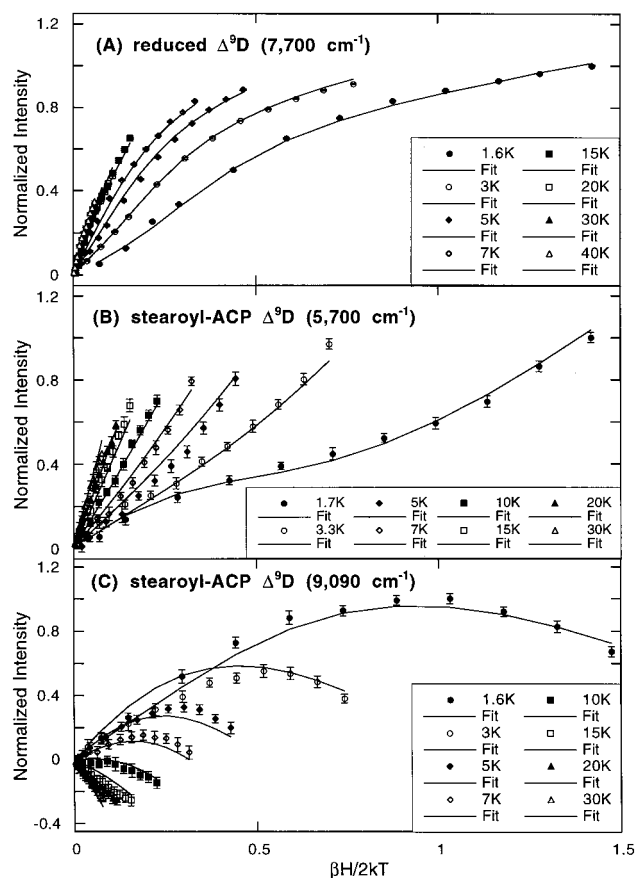
Figure 6. Saturation-magnetization behavior of the MCD signal in the ligand-field region for (A) reduced Δ^9-desaturase at 7700 cm^{-1}, (B) stearoyl-ACP Δ^9-desaturase at 5700 cm^{-1}, and (C) stearoyl-ACP Δ^9-desaturase at 9090 cm^{-1}. The intensity amplitude (symbols) for a range of magnetic fields (0–7.0 T) at a series of fixed temperatures is plotted as a function of $\beta H/2kT$. The fit to the VTVH MCD data (solid line) was obtained using eq 6 with the parameters given in Table 2. Error bars are included; in the case of reduced Δ^9-desaturase the error bars for individual points are smaller than the symbol size used.

lent, since a single Fe(II) atom cannot have more than two ligand-field transitions above 5000 cm^{-1}. There is only one transition observed at >8000 cm^{-1}, indicating that neither iron can be 6-coordinate. The presence of a high-energy transition at ~9000 cm^{-1} requires that one of the irons (Fe1) is 5-coordinate. Compared to the square pyramidal structure observed for the reduced form, the highest energy transition has decreased in energy (~9000 cm^{-1} vs ~10 000 cm^{-1} in reduced Δ^9D, Figure 2), and the energy splitting of the highest two transitions has also decreased (~1700 cm^{-1} vs ~2900 cm^{-1} in reduced Δ^9D, Figure 2). From the LF calculation (vide supra), this would require a further distortion of the *xy*-plane, which is already extremely distorted in Figure 3B. Alternatively, in a trigonal bipyramidal spectrum, there can be a transition in the high-energy region at ~9000 cm^{-1}, and the next ligand-field transition will be at <5000 cm^{-1}, below the range of our near-IR instrument. This would generate a negative zero-field splitting ($-D$), which is consistent with the results obtained from the ground-state analysis (vide infra). Thus, Fe1 is best described as 5-coordinate with a distorted trigonal bipyramidal geometry, and the transition at ~9000 cm^{-1} is associated with this iron. The other two transitions at ~7500 and ~5500 cm^{-1} are correlated with the second iron (Fe2), and the energies of these transitions indicate that Fe2 has a distorted tetrahedral structure, which would generate a positive zero-field splitting ($+D$).

To summarize the excited-state studies, the active site of reduced Δ^9D contains two equivalent 5-coordinate irons with distorted square pyramidal geometries (a two-in–two-out equatorial distortion). Substrate binding significantly alters the geometric structure of both irons. One of the irons remains 5-coordinate, but distorts toward trigonal bipyramidal. More dramatically, the other iron becomes 4-coordinate, implying that the substrate binding induces an additional open coordination position which correlates with the increased O$_2$ reactivity.

B. Ground State. 1. Reduced Δ^9D. The MCD intensity for reduced Δ^9D increases as temperature decreases, indicating that these transitions are MCD *C*-terms associated with paramagnetic doublets that are split by a magnetic field. Figure 6A shows the VTVH MCD saturation-magnetization curves of reduced Δ^9D measured at 7700 cm^{-1} (symbols, with their standard deviations given by the error bar for each datum point). These curves are nested, with the high-temperature data offset from the low-temperature data when the isotherms are plotted as a function of $\beta H/2kT$. This is associated with rhombic zero-field splitting of a non-Kramers doublet ground state and arises from nonlinear field-induced mixing between the sublevels of the doublet. In addition, the slope change observed in the low-field region (up to ~0.7 T) of the lowest temperature data implies that there is a change of the ground state with application of a magnetic field.

To analyze the ground state associated with the data on reduced Δ^9D, we consider the electronic structure of a coupled binuclear ferrous system. A high-spin ferrous ion has an $S = 2$ ground state with $M_s = 0, \pm1$, and ±2. This 5-fold degeneracy will split due to zero-field splitting, which is defined by axial (D) and rhombic (E) spin-Hamiltonian parameters. In an exchange-coupled system, the two ferrous ions can also interact through bridging ligands to give $S_{tot} = |S_1 + S_2| ... |S_1 - S_2| = 4, 3, 2, 1$, and 0 levels. These levels are split by the exchange coupling $H = -2JS_1S_2$ to generate $(2S_{tot} + 1)M_s$ degenerate levels, which are further split in energy by zero-field splitting. Since the magnitudes of D and J are comparable in binuclear non-heme ferrous systems, the combined effects should be considered. Equation 1 shows a simplified expression of the

$$
\begin{aligned}
H = &-2J\hat{S}_1\cdot\hat{S}_2 + D_1(\hat{S}^2_{z1} - 1/3S(S+1)) + \\
&E_1(\hat{S}^2_{x1} - \hat{S}^2_{y1}) + D_2(\hat{S}^2_{z2} - 1/3S(S+1)) + \\
E_2(\hat{S}^2_{x2} - &\hat{S}^2_{y2}) + g_{z1}\beta H_z\hat{S}_{z1} + g_{x1}\beta H_x\hat{S}_{x1} + g_{y1}\beta H_y\hat{S}_{y1} + \\
&g_{z2}\beta H_z\hat{S}_{z2} + g_{x2}\beta H_x\hat{S}_{x2} + g_{y2}\beta H_y\hat{S}_{y2} \quad (1)
\end{aligned}
$$

spin Hamiltonian for a general non-heme biferrous system, which operates on the uncoupled basis set $|S_1, S_2, M_{s1}, M_{s2}\rangle$, where the subscripts indicate the two ferrous centers. J is the isotropic exchange coupling between the two iron sites and D_1, D_2, E_1, and E_2 are the axial and rhombic ZFS parameters for each iron arising from local spin–orbit coupling. Zeeman terms ($g_{z1}\beta H_{z1}S_{z1}$, etc.) are also included, where the *g* value can be coupled to the ZFS parameters using ligand-field theory as given in eqs 2a and 2b.[58] λ is the Fe(II) ground-state spin–orbit coupling constant (~100 cm^{-1}) and k^2 is the Stevens orbital reduction factor, which is <1 due to covalency.

Several additional terms should be, in principle, included in eq 1, including the magnetic dipolar (D_{dip}), anisotropic (D_{aniso}), and antisymmetric (*d*) exchange interactions between the two irons. D_{dip} arises from the electron spin dipolar–spin dipolar

---

(58) Note that in principle one should solve the complete $^5T_{2g}$ Hamiltonian rather than a spin Hamiltonian since there is orbital as well as spin angular momentum. However, near the rhombic limit appropriate for these sites (vide infra) these give similar results. See ref 66.

$$D_{\mathrm{Fe^{2+}}} = \frac{-k^2\lambda}{4}(g_{x\mathrm{Fe^{2+}}} + g_{y\mathrm{Fe^{2+}}} - 2g_{z\mathrm{Fe^{2+}}}) \qquad (2a)$$

$$E_{\mathrm{Fe^{2+}}} = \frac{-k^2\lambda}{4}(g_{y\mathrm{Fe^{2+}}} - g_{x\mathrm{Fe^{2+}}}) \qquad (2b)$$

interaction between the irons at a distance r and can be estimated from eq 3,[59,60] where μ_1 and μ_2 represent the magnetic dipole

$$D_{\mathrm{dip}} = \frac{\mu_1\mu_2}{r^3}S_1S_2 \qquad (3)$$

moments of the two irons. The D_{aniso}, sometimes called the pseudodipolar interaction, derives from the combined effect of the single-iron spin−orbit coupling of ligand-field excited states with the ground state and the exchange interaction between the magnetic centers. Its magnitude can be estimated from[61−63]

$$D_{\mathrm{aniso}} \approx \left(\frac{\lambda}{\Delta}\right)^2 J \approx \left(\frac{\Delta g}{g}\right)^2 J \qquad (4)$$

where λ is the spin−orbit coupling constant, Δ is the energy difference between the coupled ground and excited electronic states, and J is the isotropic exchange coupling constant between an excited state on one iron and the ground state on the second iron. The d is operative only when the binuclear site is of low symmetry. This interaction also originates from the combined effect of the spin−orbit and exchange couplings; its magnitude can be estimated from[61−63]

$$d \approx \left(\frac{\lambda}{\Delta}\right)J \approx \left(\frac{\Delta g}{g}\right)J \qquad (5)$$

D_{dip} and D_{aniso} are all purely anisotropic; thus, they only contribute to the dimer ZFS. For the biferrous site of $\Delta^9\mathrm{D}$, D_{dip} values are estimated to be $\sim$0.09 cm^{-1} (from eq 3 with $r = \sim$4.2 Å). D_{aniso} and d are a few percent of the isotropic exchange coupling J. Since J is small (*vide infra*), they will have negligible effects compared to the magnitude of the ZFS from each iron ($\sim$5−10 cm^{-1}). Thus, the isotropic exchange coupling J and the ZFS parameters D and E from each iron (eq 1) will be the dominant terms describing the binuclear ferrous ground state with carboxylate bridges.

Application of eq 1 to the uncoupled basis generates a 25 × 25 matrix. Diagonalization of this matrix in zero magnetic field gives the wave functions of the binuclear ferrous spin states and their energies, which are dependent on the relative magnitudes of the exchange coupling and the ZFS. The magnitude of D is constrained to be less than |15| cm^{-1} (the largest value from model systems and ligand-field calculations); the maximum |E/D| is 1/3.

From the excited-state analysis and crystallographic results, reduced $\Delta^9\mathrm{D}$ has two approximately equivalent 5-coordinate irons in a distorted square pyramidal environment. Therefore, D_1 and D_2 are treated as equal. On the basis of model data,[51] a reasonable range for |D| for this geometry is $\sim$10−15 cm^{-1} with the sign dependent on the strength of the axial ligand

(59) Kahn, O. *Molecular Magnetism*; VCH Publishers: New York, 1993; Chapter 7.
(60) Weltner, W., Jr. *Magnetic Atoms and Molecules*; Dover Publications: New York, 1983; pp 304−339
(61) Bencini, A.; Gatteschi, D. *Electron Paramagnetic Resonance of Exchanged Coupled System*; Springer-Verlag: Berlin-Heidelberg, 1990; Chapter 2.
(62) Moriya, T. In *Magnetism*; Rado, G. T., Suhl, H., Eds.; Academic Press Inc.: New York and London, 1963; Vol. 1, pp 85−124.
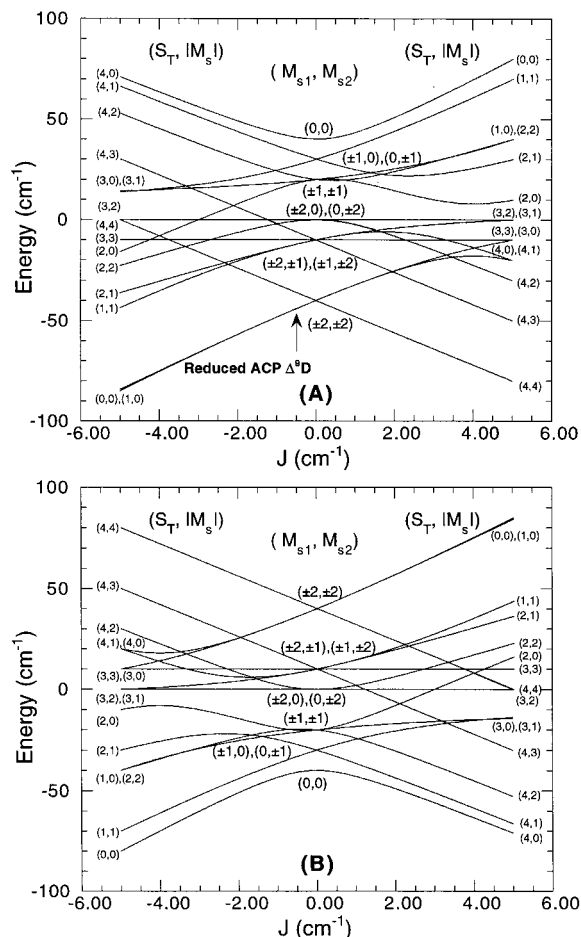(63) Moriya, T. *Phys. Rev.* **1960**, *120*, 91−98.

Figure 7. Correlation diagram of the energy levels of the binuclear ferrous ground state including exchange coupling and single-site ZFS. In (A) negative axial ZFS parameters (D) of the two iron atoms are held constant and equal ($D_1 = D_2 = -10$ cm^{-1}). In (B) positive axial ZFS parameters (D) on the two iron atoms are held constant and are constrained to be equal ($D_1 = D_2 = +10$ cm^{-1}). The exchange coupling (J) is varied from −5 to +5 cm^{-1}. The central portion gives the pure ZFS limit with states labeled with M_s values for each uncoupled Fe(II) (M_{s1}, M_{s2}). The right side indicates a ferromagnetic interaction ($J > 0$) between the ferrous atoms, and the left an antiferromagnetic interaction ($J < 0$). The spin Hamiltonian used for calculating the levels is given in eq 1, with $E_1 = E_2 = 0$ and $H_x = H_y = H_z = 0$.

(negative for weak axial ligation, as given by the ligand-field calculation in Figure 3C where the energies of the d_{xz} and d_{yz} orbitals are below that of the d_{xy} orbital). Equation 1 was first evaluated with $D_1 = D_2 = -10$ cm^{-1} and axial ($E_1 = E_2 = 0$) symmetry for a range of J values from −5 to +5 cm^{-1} (Figure 7A). The center of the figure gives the limiting case where two $S = 2$ Fe(II) ions have no exchange coupling interaction, but large ZFS (indicated by uncoupled basis functions (M_{s1}, M_{s2})). These states split in energy when the two Fe(II) ions are allowed to couple (|J| > 0), resulting in dimer wave functions expressed as (S_{tot}, |M_s|). The left side of the figure gives antiferromagnetic coupling ($J < 0$), which generates two degenerate (S_{tot}, $\pm M_s$) = (0, 0)/(1, 0) levels as the ground state and (4, $\pm$4) or (1, $\pm$1) as the first excited state depending on the magnitude of J. The right side gives ferromagnetic coupling ($J > 0$), producing an (S_{tot}, $\pm M_s$) = (4, $\pm$4) ground state and different excited states dependent on the magnitude of J. Thus, when $J < 0$, the ground state is a singlet which would not show MCD intensity at low temperature, while for $J > 0$ the ground state will be paramagnetic with a $g_{||} = 16$. Varying the magnitude of $D_1 = D_2$ from −10 to −15 or −5 cm^{-1} changes the energy differences
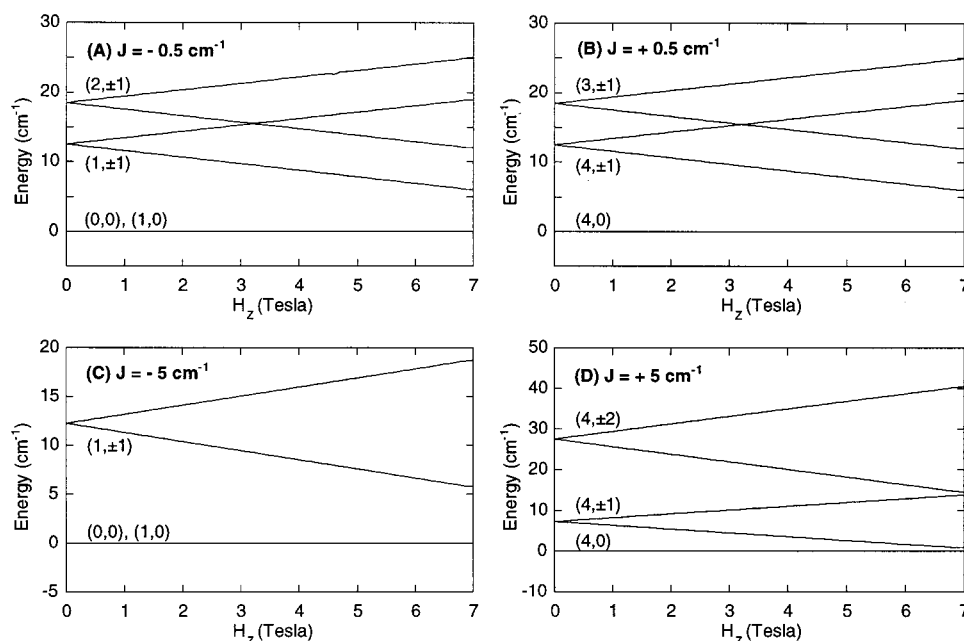
Figure 8. Representative correlation diagrams of the energy splittings of the binuclear ferrous ground and excited sublevels with positive ZFS in the presence of a magnetic field along the z-axis. The axial and rhombic ZFS parameters on the two iron atoms are held constant and are constrained to be equal ($D_1 = D_2 = +10$ cm^{-1}, $E_1 = E_2 = 0$). The exchange coupling (J) is fixed at (A) $J = -0.5$ cm^{-1}, (B) $J = +0.5$ cm^{-1}, (C) $J = -5$ cm^{-1}, and (D) $J = +5$ cm^{-1}. The ground and excited sublevels are labeled as $\langle S_{\text{tot}}, \pm M_s \rangle$. The spin Hamiltonian used for calculating the levels is given in eq 1, with $H_x = H_y = 0$ and H_z varied from 0 to 7 T.

among the states. Turning on rhombicity removes all degeneracy and leads to mixed wave functions. However, neither of these perturbations affects the energy order.

Changing to a positive ZFS dramatically alters the energy diagram. Figure 7B presents the energy diagram for $D_1 = D_2 = +10$ cm^{-1} with an axial ($E_1 = E_2 = 0$) symmetry over a range of J values from -5 to $+5$ cm^{-1}. The right-hand side gives ferromagnetic coupling ($J > 0$) with an ($S_{\text{tot}}, \pm M_s$) = (4, 0) as the ground state and an ($S_{\text{tot}}, \pm M_s$) = (4, ±1) as the first excited state regardless of the magnitude of J. The left-hand side gives antiferromagnetic coupling ($J < 0$) with ($S_{\text{tot}}, \pm M_s$) = (0, 0) as the ground state. ($S_{\text{tot}}, \pm M_s$) = (1, ±1) is the first excited state independent of the magnitude of J. Varying the magnitude of $D_1 = D_2$ from -10 to -15 or -5 cm^{-1} changes the energy differences among the states, and turning on the rhombicity (to $|E/D| = 1/3$) removes all degeneracy and produces mixed wave functions, but neither affects the energy order.

Therefore, for the ground state of reduced Δ⁹D, there are four possible combinations of D and J. We can rule out $D < 0$, $J > 0$ (ground state ($S_{\text{tot}}, \pm M_s$) = (4, ±4)) for two reasons: (1) the VTVH MCD data (Figure 6A) do not show $g_{||} = 16$ saturation behavior, and (2) there is no EPR signal. To evaluate the other three possibilities, a series of calculations were performed over a range of J values for the axial and rhombic cases in the presence of a magnetic field of up to 7 T. No significant difference is observed when $|D|$ is varied. Turning on the rhombicity lowers the symmetry such that the states do not cross. VTVH MCD data show a slope change in the low-temperature–low-field region (Figure 6A) which indicates a change in the ground state upon increasing the magnetic field. Figure 8 gives representative energy level diagrams for $D_1 = D_2 = 10$ cm^{-1} and negative or positive J values with varying the magnetic field along the z-axis. Figure 9 shows the representative energy level diagrams for $D_1 = D_2 = -10$ cm^{-1} and negative J values with varying the magnetic field along the z-axis. A magnetic field induced crossover of a low-lying excited state to become

the ground state is not observed when $D > 0$ (Figure 8); thus, the ZFS for each iron is negative, and the two irons are antiferromagnetically coupled ($D < 0$, $J < 0$; ground state ($S_{\text{tot}}, \pm M_s$) = (1, 0), Figure 7A, left). When $-J$ is relatively large, above 2 cm^{-1} (Figure 9C,D), the energy splitting induced by a magnetic field of up to 7 T is not large enough to change the ground state which remains $M_s = 0$. However, when J is small relative to the ZFS ($-J = 0.5$ cm^{-1}, Figure 9A), a crossover of the energy levels is observed at low magnetic field. This changes the ground state from $M_s = 0$ to $M_s = \pm 4$, which is consistent with the VTVH MCD behavior (vide infra). Notice that turning on the rhombicity (Figure 9B) retains the energy order of the ground and excited states at 0 T. However, when the magnetic field is increased, one $M_s = 0$ state and the $M_s = -4$ states mix which gives the ground-state $M_s = -4$ character, and the $M_s = -4$ sublevel gains $M_s = 0$ character. Varying $D_1 = D_2$ by ±5 cm^{-1} does not significantly perturb the energy diagrams shown in Figures 8 and 9. Energy splittings along the x- and y-axis were also examined, and no magnetic field induced crossover of a low-lying excited state occurs. Thus, the axial ZFS parameters and the upper limit of the $-J$ for reduced Δ⁹D can be estimated as $D_1 = D_2 = \sim -10 \pm 5$ cm^{-1} and $-J < \sim 2$ cm^{-1}.

The analysis was also performed including noncollinearity of the ZFS tensors of the two ferrous sites. On the basis of the crystal structure,[17] reduced Δ⁹D has a N$_{\text{His}}$–Fe$_1$–Fe$_2$–N$_{\text{His}}$ dihedral angle (β) of $\sim 45°$ referenced to the plane perpendicular to the Fe–Fe axis. Thus, the energy level diagram from eq 1 was also generated including $\beta = 45°$ and fixing all other parameters. Compared to Figure 7, the results indicate that the order of the sublevels within the energy range of interest (up to ~ 40 cm^{-1}) does not change, but the energy differences do vary. The energy level diagram is given in Supporting Information Figure S1.

To test the energy diagram in Figure 9B and obtain a more accurate estimate of the ground-state spin-Hamiltonian parameters, the VTVH MCD data were fit using the MCD intensity
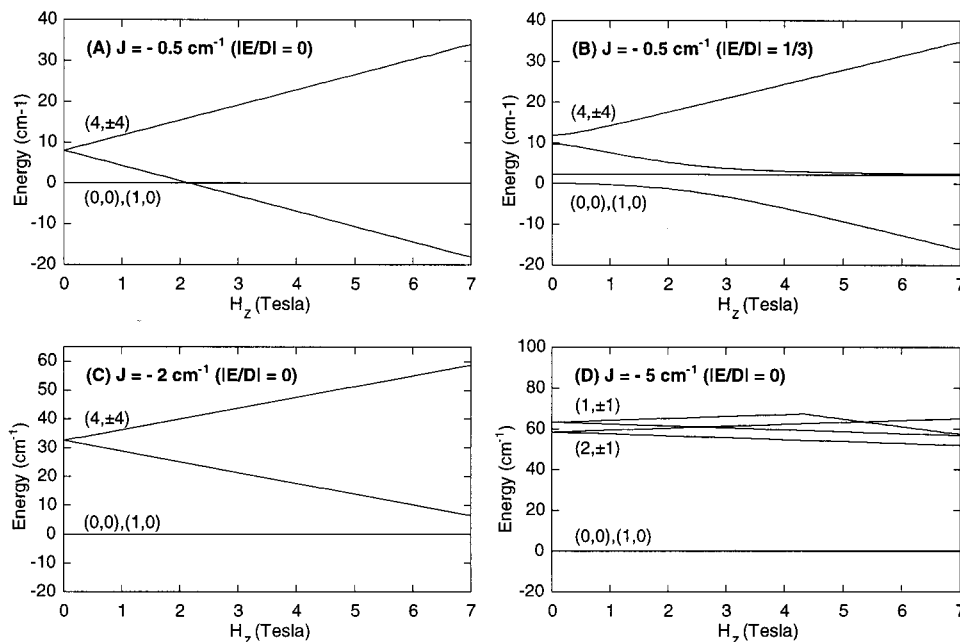
Figure 9. Representative correlation diagrams of the energy splittings of the binuclear ferrous ground and excited sublevels with negative ZFS in the presence of a magnetic field along the *z*-axis. The axial ZFS parameters on the two iron atoms are held constant and constrained to be equal ($D_1 = D_2 = -10$ cm^{-1}). The rhombic ZFS (E) and the exchange coupling (J) are fixed at (A) $J = -0.5$ cm^{-1}, $|E/D| = 0$, (B) $J = -0.5$ cm^{-1}, $|E/D| = 1/3$, (C) $J = -2$ cm^{-1}, $|E/D| = 0$, and (D) $J = -5$ cm^{-1}, $|E/D| = 0$. The ground and excited sublevels are labeled as $\langle S_{tot}, \pm M_s \rangle$. The spin Hamiltonian used for calculating the levels is given in eq 1, with $H_x = H_y = 0$ and H_z varied from 0 to 7 T.

expression for a non-Kramers system, allowing for the effects of a linear *B*-term from field-induced mixing between states and the presence of excited sublevels of the ground state, eq 6.[64-66]

$$\Delta\epsilon = \sum_i \left[(A_{\text{sat lim}})_i \left(\int_0^{\pi/2} \frac{\cos^2\theta \sin\theta}{\Gamma_i} g_{||i}\beta H\alpha_i \, d\theta - \sqrt{2}\frac{M_z}{M_{xy}} \int_0^{\pi/2} \frac{\sin^3\theta}{\Gamma_i} g_{\perp i}\beta H\alpha_i \, d\theta \right) + B_i H\gamma_i \right] \quad (6)$$

$$\Gamma_i = \sqrt{\delta_i^2 + (g_{||i}\beta H\cos\theta)^2 + (g_{\perp i}\beta H\sin\theta)^2}$$

$$\alpha_i = \frac{e^{-(E_i - \Gamma_i/2)/kT} - e^{-(E_i + \Gamma_i/2)/kT}}{\sum_j e^{-(E_j - \Gamma_j/2)/kT} + e^{-(E_j + \Gamma_j/2)/kT}}$$

$$\gamma_i = \frac{e^{-(E_i - \delta_i/2)/kT} + e^{-(E_i + \delta_i/2)/kT}}{\sum_j e^{-(E_j - \beta_j/2)/kT} + e^{-(E_j + \delta_j/2)/kT}}$$

$(A_{\text{sat lim}})_i$, B_i, δ_i, $g_{||i}$, and $g_{\perp i}$ are the *C*-term and *B*-term MCD intensities, the rhombic ZFS, and the dimer *g* values of the *i*th doublet, respectively. E_i is the energy of the *i*th sublevel, and the energy of the ground state is defined as zero. The Boltzmann population over all states has been included in both the *C*-term and the *B*-term intensities as the factors α_i and γ_i, respectively. *H* is the applied magnetic field, *k* is the Boltzmann constant, and M_z and $M_{x,y}$ are the transition dipole moments for the directions indicated.

(64) Browett, W. R.; Fucaloro, A. F.; Morgan, T. V.; Stephens, P. J. *J. Am. Chem. Soc.* **1983**, *105*, 1868−1872.

(65) Bennett, D. E.; Johnson, M. K. *Biochim. Biophys. Acta* **1987**, *911*, 71−80.

(66) Solomon, E. I.; Pavel, E. G.; Loeb, K. E.; Campochiaro, C. *Coord. Chem. Rev.* **1995**, *144*, 369−460.

The energy levels from the spin-Hamiltonian analysis (vide supra), two MCD inactive singlets ($M_s = 0$) and an $M_s = \pm 4$ doublet, were used to fit the VTVH MCD data for reduced Δ^9D (Figure 6A). The adjustable parameters $A_{\text{sat lim}}$, *B*, δ, and the energy of the $M_s = \pm 4$ doublet were allowed to float ($A_{\text{sat lim}} = 0$ for $M_s = 0$). The $g_{||}$ for the $M_s = \pm 4$ doublet was fixed at 16.0. Inclusion of additional $g_\perp$ and polarization ratio $M_z/M_{x,y}$ parameters for the $M_s = \pm 4$ doublet did not significantly improve the fit. The best fit (included as solid lines in Figure 6A) gives an $M_s = \pm 4$ doublet ($g_{||} = 16.0$) at ~11 cm^{-1} having $\delta = $ ~2.0 cm^{-1} with an $M_s = 0$ state located ~2 cm^{-1} above the $M_s = 0$ ground state. Figure 10A gives the qualitative energy level diagram for reduced Δ^9D generated from the best fit of the VTVH MCD analysis. This result is consistent with Figure 9B, indicating that the irons are rhombic. It further supports the fact that the low-lying $M_s = \pm 4$ doublet strongly perturbs the ground state in the low-field region, resulting in a significant amount of $M_s = \pm 4$ character. The excited sublevel energies obtained from the VTVH MCD fit, correlated with the energy level diagram shown in Figure 7A, indicate that reduced Δ^9D is required to have two negative $D_1 = D_2 = $ ~-10 ± 5 cm^{-1} and $0 < -J < $ ~1.0 cm^{-1}.

In the above analysis, second-order contributions have been included via the *B*-term contribution to MCD intensity. The VTVH MCD intensity was also simulated by calculations using the dimer wave functions from eq 1 and using the fact that the MCD intensity is proportional to the spin-expectation values of the single iron center being studied by MCD projected on the dimer states.[67] A series of simulations were performed with a number of combinations of D_1, D_2, J, and the effective transition moment products M_{xy}, M_{xz}, and M_{yx}. The results indicate that with $D_1 = D_2 = $ ~-15 cm^{-1}, $-J = $ ~0.5 cm^{-1}, and the 7700 cm^{-1} MCD transition pure *x,y* polarized, the simulation demonstrates a good agreement with the VTVH MCD data of the reduced Δ^9D shown in Figure 6A (see the Supporting Information, Figure S8A). These ground-state

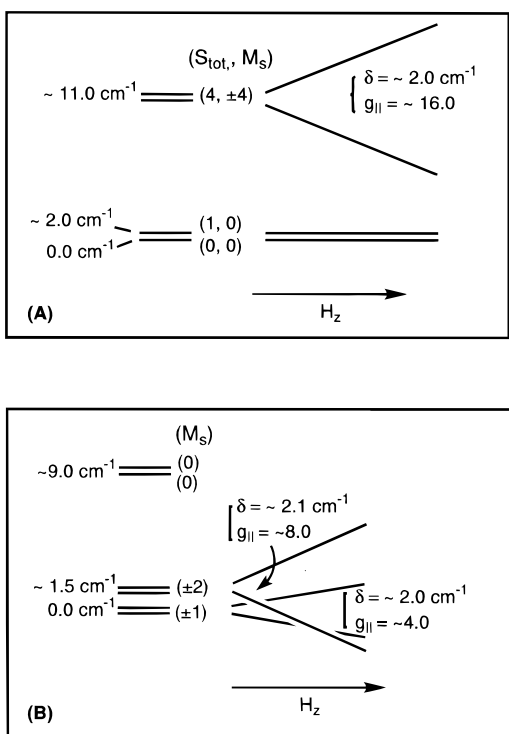(67) Neese, F.; Solomon, E. I. *Inorg. Chem.*, submitted for publication.

Figure 10. Ground-state energy level diagrams for (A) reduced Δ^9-desaturase and (B) stearoyl-ACP Δ^9-desaturase obtained from the best fit to the complete VTVH MCD data. Parentheses indicate the spin states expressed as (S_{tot}, M_s) for the ground and excited states.

Table 2. Summary of MCD Parameters for the Ground and Excited States of Reduced Binuclear Non-Heme Δ^9-Desaturase (Reduced Δ^9D)

	reduced Δ^9D (7700 cm^{-1})		
	$M_s = 0$	$M_s = 0$	$M_s = \pm 4$
$g_{\|\|}$			16.02 ± 0.5
δ (cm^{-1})			2.07 ± 0.2
A			1.62 ± 0.1
B	0.02 ± 0.01	0.08 ± 0.01	-0.05 ± 0.02
energy (cm^{-1})	0.0 ± 0.0	1.97 ± 0.2	10.57 ± 0.2

Table 3. Summary of Spin-Hamiltonian Parameters for Reduced Binuclear Non-Heme Δ^9-Desaturase (Reduced Δ^9D) and Substrate-Bound Δ^9-Desaturase (Stearoyl-ACP Δ^9D)

	reduced Δ^9D (7700 cm^{-1})	stearoyl-ACP Δ^9D (5700, 9090 cm^{-1})
$-J$ (cm^{-1})	$< \sim 1.0$	$< \sim 2.5$
D_1 (cm^{-1})	$-15 < D_1 < -5$	$-15 < D_1 < -5$
D_2 (cm^{-1})	$-15 < D_2 < -5$	$+3 < D_2 < +12$

parameters are also consistent with the ones obtained from the spin-Hamiltonian analysis and VTVH MCD fit using eq 6 described above. Tables 2 and 3 summarize the ground and excited sublevel parameters of reduced Δ^9D obtained from the VTVH MCD and spin-Hamiltonian analyses, respectively. The error bars in Tables 2 and 3 were estimated from the average of several good fits.

In summary, the combination of VTVH MCD and spin-Hamiltonian analysis provides detailed insight into the electronic structure of reduced Δ^9D. The two irons of the active site have the same sign and approximately equal magnitudes of $D_1 = D_2 = \sim -10 \pm 5$ cm^{-1} and are weakly antiferromagnetically coupled with $-J = < \sim 1$ cm^{-1}. This produces an energy diagram with one $M_s = 0$ level as the ground state and another $M_s = 0$ plus an $M_s = \pm 4$ doublet as excited sublevels at ~ 2

Table 4. Summary of MCD Parameters for the Ground and Excited States of Reduced Binuclear Non-Heme Substrate-Bound Δ^9-Desaturase (Stearoyl-ACP Δ^9D) at (A) 5700 cm^{-1} and (B) 9090 cm^{-1}

(A) Stearoyl-ACP Δ^9D (5700 cm^{-1})				
	$M_s = \pm 1$	$M_s = \pm 2$	$M_s = 0$	$M_s = 0$
$g_{\|\|}$	3.93 ± 0.3	8.02 ± 0.3		
δ (cm^{-1})	1.97 ± 0.2	1.99 ± 0.2		
A	1.31 ± 0.1	1.31 ± 0.1		
B	0.13 ± 0.02	-0.11 ± 0.02	8.50 ± 0.1	8.86 ± 0.1
$g_\perp$	0.00 ± 0.00	0.00 ± 0.00	–	–
$M_z/M_{x,y}$	0.00 ± 0.02	0.00 ± 0.02	–	–
energy (cm^{-1})	0.0 ± 0.0	1.34 ± 0.8	9.02 ± 0.3	9.32 ± 0.3

(B) Stearoyl-ACP Δ^9D (9090 cm^{-1})				
	$M_s = \pm 1$	$M_s = \pm 2$	$M_s = 0$	$M_s = 0$
$g_{\|\|}$	3.93 ± 0.3	8.02 ± 0.3		
δ (cm^{-1})	1.97 ± 0.2	1.99 ± 0.2		
A	-0.71 ± 0.2	5.66 ± 0.2		
B	-0.27 ± 0.2	-0.19 ± 0.1	14.58 ± 0.5	14.28 ± 0.4
$g_\perp$	1.00 ± 0.0	1.00 ± 0.0		
$M_z/M_{x,y}$	2.05 ± 0.10	2.05 ± 0.10		
energy (cm^{-1})	0.0 ± 0.0	1.34 ± 0.2	9.02 ± 0.3	9.32 ± 0.3

and ~ 11 cm^{-1} above the ground state, respectively. Application of a magnetic field splits the $M_s = \pm 4$ doublet. The $M_s = -4$ sublevel interacts with the two $M_s = 0$ states at ~ 1 T, which introduces increasing $M_s = -4$ character into the lower sublevel as the magnetic field increases.

2. Stearoyl-ACP Δ^9D. Parts B and C of Figure 6 present the VTVH MCD data for the stearoyl-ACP Δ^9D complex collected at 5700 and 9090 cm^{-1}. Dramatic changes in the saturation-magnetization behavior are observed upon the addition of the substrate compared to that of the reduced form in Figure 6A. Figure 6B shows an "inverse saturation" behavior, in which the slope changes at ~ 5 T and the MCD signal increases with increasing magnetic field. This indicates that, at ~ 5 T, the ground state has changed to one with a larger $g_{\|\|}$ value (i.e., a larger M_s), which is consistent with the crossover of a low-lying excited state to become the ground state in the presence of a magnetic field. The lowest temperature (1.6 K) data collected at 5700 cm^{-1} were fit first using eq 6. The $(A_{sat\,lim})_0$, B_0, δ_0, and $g_{\|\|}$ are adjustable parameters, while $g_\perp$ and the polarization ratio $M_z/M_{x,y}$ were initially fixed at zero but later allowed to float to improve the fit. A good fit was obtained up to ~ 5 T with one non-Kramers doublet having $g_{\|\|} = 3.9$ and $\delta_0 = \sim 2.0$ cm^{-1}, indicating an $M_s = \pm 1$ ground state. The inclusion of a second doublet with $g_{\|\|} = 8.02$ and $\delta_1 = \sim 2.1$ cm^{-1}, associated with an $M_s = \pm 2$ state, at ~ 1.5 cm^{-1} above the $M_s = \pm 1$ state greatly improves the fit in the high-field region of the 1.6 K data and to the saturation-magnetization curves for temperatures up to 7 K. Allowing for the effects of z-polarization ($g_\perp \neq 0$) in the analysis does not significantly improve the fit. At temperatures above 7 K, the fit consistently overestimates the intensity of the MCD signal, indicating the presence of at least one more excited sublevel. The effect of additional excited states on the VTVH MCD data was included in the fit by fixing the best fit parameters obtained as described above for the $M_s = \pm 1$ and $M_s = \pm 2$ doublets, and allowing the parameters associated with the additional excited states to float. Inclusion of two $M_s = 0$ sublevels ($A_{sat\,lim}$ and $g_{\|\|} = 0$, energies and B-term intensities allowed to vary to obtain a good fit) at ~ 9 cm^{-1} above the $M_s = \pm 1$ doublet significantly improves the fit. The parameters obtained are given in Table 4. A large B-term parameter for the two $M_s = 0$ states is likely due to their magnetic field induced interaction with the high-energy $M_s = \pm 3$ doublet (vide infra). Thus, the VTVH MCD

fit of the 5700 cm^{-1} band shows that the coupled active site has an $M_s = \pm 1$ non-Kramers doublet as its ground state, an $M_s = \pm 2$ doublet at ~ 2 cm^{-1}, and two other $M_s = 0$ singlets at ~ 9 cm^{-1} above the ground sublevel. The low-lying $M_s = \pm 2$ excited state crosses over the $M_s = \pm 1$ ground state in the presence of a magnetic field, causing a change in the ground state as observed in the midfield region of the lowest temperature (1.6 K) curve in the VTVH MCD data shown in Figure 6B, resulting in the inverse saturation behavior.

Although the magnetization-saturation behavior observed at 9090 cm^{-1} is dramatically different from the data collected at 5700 cm^{-1}, it must reflect the same ground and excited sublevels of the substrate-bound form.[68] Thus, the energy levels obtained from the best fit for the 5700 cm^{-1} band were used to fit the VTVH MCD data collected at 9090 cm^{-1} (Figure 6C). The δ and $g_{||}$ of the $M_s = \pm 1$ and $M_s = \pm 2$ doublets, and the energies of all four states, were fixed at the values described above, and the $A_{\text{sat lim}}$ and B-term parameters ($A_{\text{sat lim}} = 0$ for the singlets) for each sublevel were allowed to vary to fit the data. A large polarization ratio $M_z/M_{x,y} = \sim 2.0$ gives a good fit with the different magnetization-saturation behavior observed from this band. For z-polarized transitions, $g_\perp$ now strongly affects the magnetic field behavior and is much smaller than $g_{||}$. $g_\perp$ was set at 1.0 for the two doublets.

A series of VTVH MCD simulations (vide supra) were also performed with a number of combinations of D_1, D_2, J, and the effective transition moment products M_{xy}, M_{xz}, and M_{yx}. The results indicate that, with $D_1 = \sim -7$ cm^{-1}, $D_2 = \sim +3$ cm^{-1}, and $-J = \sim 2.5$ cm^{-1}, the simulations give a good agreement with the VTVH MCD data collected at both 5700 and 9090 cm^{-1} from substrate-bound Δ^9D shown in Figure 6B,C (see the Supporting Information, Figure S8B,C). Note that the simulations for both bands can be obtained with the same set of ground-state parameters but different polarization components, which is consistent with the results from the VTVH MCD and spin-Hamiltonian analyses.

Table 4 presents a summary of the parameters for the ground and excited states for the stearoyl-ACP Δ^9D analysis obtained from the VTVH MCD analysis. The error bars were estimated from the average of several good fits. Figure 10B shows the qualitative energy level diagram for stearoyl-ACP Δ^9D generated from the best fit obtained from the VTVH MCD.

The spin-Hamiltonian analysis described above for reduced Δ^9D was then applied to investigate the experimental sublevel splittings for stearoyl-ACP Δ^9D in terms of exchange coupling (J) and zero-field splitting. From the excited-state analysis summarized in Figure 6B,C and Table 4, the active site consists of one iron (Fe1) with a distorted trigonal bipyramidal geometry (9090 cm^{-1}) and the other (Fe2) with a distorted 4-coordinate environment (5700 and 7500 cm^{-1}); thus, D_1 is negative, D_2 is positive, and $|D_1| > |D_2|$. Therefore, a series of calculations using eq 1 were performed varying the D_1 from -15 to -5 cm^{-1} and the D_2 from $+10$ to $+5$ cm^{-1} for both axial ($|E/D| = 0$) and rhombic ($|E/D| = 1/3$) symmetry with J values varying from -5 to $+5$ cm^{-1}. Figure 11 gives a representative energy level diagram with $D_1 = -10$ cm^{-1}, $D_2 = +5$ cm^{-1}, $E_1 = E_2 = 0$, and $J = -5$ to $+5$ cm^{-1}. The center of the figure gives the limiting case where the two $S = 2$ Fe(II) atoms have no exchange coupling. These uncoupled (M_{s1}, M_{s2}) states split when $|J| > 0$. The right side of the figure gives ferromagnetic coupling ($J > 0$). This results in an ($S_{\text{tot}}, \pm M_s) = (2, \pm 2)$ ground state
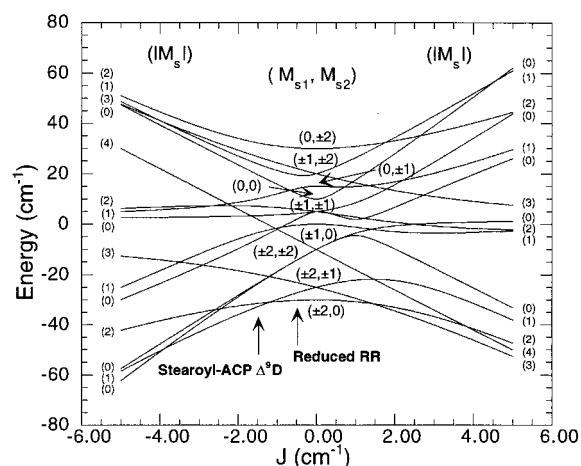
(68) VTVH data collected at 5700 and 9090 cm^{-1} were initially fit independently. $g_{||} = \sim 4$ for the ground sublevel and $g_{||} = \sim 8$ for the first excited sublevel are required for both data sets, which indicates that these two bands must reflect the same ground and excited sublevels (vide infra).

Figure 11. Correlation diagram of the energy levels of the binuclear ferrous ground state with opposite signed ZFS including exchange coupling and single-site ZFS. The axial ZFS parameters (D) on the two iron atoms are held constant and constrained to be $D_1 = +5$ cm^{-1} and $D_2 = -10$ cm^{-1}. The exchange coupling (J) is varied from -5 to $+5$ cm^{-1}. The central portion gives the pure ZFS limit with states labeled with M_s values for each uncoupled Fe(II) (M_{s1}, M_{s2}). The right side indicates a ferromagnetic interaction ($J > 0$) between the ferrous atoms, and the left side an antiferromagnetic interaction ($J < 0$). The spin Hamiltonian used for calculating the levels is given in eq 1, with $E_1 = E_2 = 0$ and $H_x = H_y = H_z = 0$.

when J is small but changes to $(3, \pm 3)$ when $J > \sim 1$ cm^{-1}, with different excited states dependent on the magnitude of J. The left side gives antiferromagnetic coupling ($J < 0$), which generates a ground state of $(S_{\text{tot}}, \pm M_s) = (2, \pm 2)$, $(1, \pm 1)$, or $(0, \pm 0)$ as $-J$ increases. Varying the magnitude of D_1 and D_2 within the range given above but retaining $|D_1| > |D_2|$ changes the energy differences among the states. Turning on the rhombicity removes all the degeneracy and leads to mixed wave functions. However, neither affects the energy order.

From the VTVH MCD analysis, the ground state of the stearoyl-ACP Δ^9D has $g_{||} = 4$, indicating that it is an $M_s = \pm 1$ doublet, which falls on the left-hand side of Figure 11. This indicates that the irons are antiferromagnetically coupled with $\sim 1 < -J < \sim 3$, which gives the $M_s = \pm 2$ and two $M_s = 0$ excited sublevels that can be thermally populated within the temperature range of the VTVH MCD data (~ 25 K, Figure 6B,C). Varying the magnitude of D_1 and D_2 within the range given above expands the range of $-J$ to $\sim 1 < -J < \sim 4$. The energy order of the three excited states varies depending on the magnitude of J. However, the VTVH MCD analysis indicates that the $M_s = \pm 2$ doublet is at ~ 1.5 cm^{-1} and the two $M_s = 0$ states are at ~ 9.0 cm^{-1}, which requires a $-J$ of $< \sim 2$ cm^{-1} with $-12 < D_1 < -5$ cm^{-1} and $+3 < D_2 < +10$ cm^{-1}. Notice that there is another $M_s = \pm 3$ excited state very close to the two $M_s = 0$ states. The large B-term parameter for the two $M_s = 0$ states obtained from the VTVH analysis is likely due to the magnetic field induced interaction with this high-energy $M_s = \pm 3$ doublet (vide supra).

The analysis was also performed considering the possibility of noncollinearity between the ZFS tensors of the two ferrous sites. A series of energy level diagrams were generated by varying the $N_{\text{His}} - Fe_1 - Fe_2 - N_{\text{His}}$ dihedral angle (β) from $0°$ to $180°$ referenced to the plane perpendicular to the Fe−Fe axis with D_1 and D_2 of the same and opposite sign. In addition, the effects on these diagrams of a magnetic field of up to 7 T was also evaluated. The results indicate that the two ZFSs are required to have different signs to reproduce the energy order obtained from the VTVH analysis (a doublet ground state with

$g_\parallel = \sim4$ and a double excited state with $g_\parallel = \sim8$, vide supra). These energy level diagrams are given in the Supporting Information (Figures S2−S7).

In summary, the electronic structure of the active site of reduced Δ^9D is strongly perturbed by substrate binding. The combined results from the VTVH MCD and spin-Hamiltonian analysis show that the stearoyl-ACP Δ^9D has an $M_s = \pm1$ ground state with an $M_s = \pm2$ doublet and two $M_s = 0$ excited sublevels at ~1.5 and ~9.0 cm^{-1} above the ground state, and the two irons are rhombic. The exchange coupling between the two irons remains antiferromagnetic but slightly increases to $-J = <2.5$ cm^{-1}. Importantly, the ZFSs of the two irons have opposite signs as $D_1 > 0$ and $D_2 < 0$, consistent with the geometry change upon substrate binding observed from the excited-state data (vide supra). The ground-state parameters for the stearoyl-ACP Δ^9D complex obtained from the spin-Hamiltonian analysis are given in Table 3. The error bars were estimated from the average of several good fits.

Discussion

The CD and MCD data analyzed above show that the active site of reduced Δ^9D has two nearly equivalent 5-coordinate irons. The ligand-field calculation shows that the two irons have a distorted square pyramidal geometry. The combination of a weak axial interaction and a large two-in−two-out distortion in the equatorial plane causes the two observed ligand-field transitions in the near-IR region to have a smaller energy splitting than generally observed for more regular square pyramidal structures. The combination of the VTVH MCD and spin-Hamiltonian analysis shows (a) both irons have a negative ZFS of $D_1 = D_2 = \sim-10 \pm 5$ cm^{-1}, indicating that they are approximately equivalent with a weak axial square pyramidal geometry, (b) the two irons are weakly antiferromagnetically coupled with $-J = <\sim1$ cm^{-1}, resulting in an $M_s = 0$ ground state and $M_s = \pm4$ excited sublevels at ~10 cm^{-1} above the ground state in the absence of a magnetic field, (c) the iron centers are rhombic such that application of a magnetic field results in an energy splitting of the $M_s = \pm4$ doublet and its strong interaction with the $M_s = 0$ ground state, and (d) the magnitude of the observed exchange coupling constant is consistent with the presence of two μ-1,3 carboxylate bridges.[69] The CD/MCD data are consistent with the reduced Δ^9D crystal structure, and are distinct from the CD/MCD data for reduced MMO and RR.[45,70,71]

In the crystal structure shown in Figure 1, there is a vacant axial position on both irons likely accessible for dioxygen binding, yet reduced Δ^9D has low dioxygen reactivity in the absence of stearoyl-ACP. The μ-1,3 carboxylate bridges are considered as poor electron-transfer pathways for the following reasons: (1) A low exchange coupling is obtained for both reduced and substrate-bound Δ^9D, and also for other model complexes that only contain carboxylate bridges between the irons.[69] (2) A study on mixed-valent binuclear copper sites showed that the carboxylate bridge provides localized properties, while halide- and pseudohalide-bridged derivatives exhibit significant delocalization.[72,73] Thus, one possible mechanism
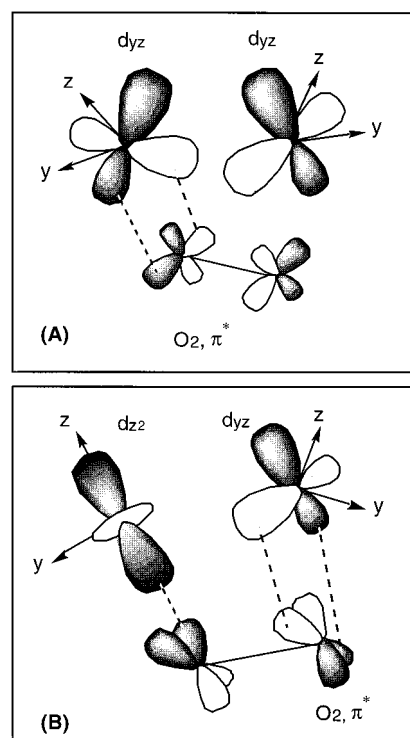
(69) Ménage, S.; Zang, Y.; Hendrich, M. P.; Que, L., Jr. *J. Am. Chem. Soc.* **1992**, *114*, 7786−7792.

(70) Pulver, S. C.; Tong, W. H.; Bollinger, M. J., Jr.; Stubbe, J.; Solomon, E. I. *J. Am. Chem. Soc.* **1995**, *117*, 12664−12678.

(71) Pulver, S. C.; Froland, W. A.; Lipscomb, J. D.; Solomon, E. I. *J. Am. Chem. Soc.* **1997**, *119*, 387−395.

(72) Himmelwright, R. S.; Eickman, N. C.; Solomon, E. I. *J. Am. Chem. Soc.* **1979**, *101*, 1576−1586.

(73) Westmoreland, T. D.; Wilcox, D. E.; Baldwin, M. J.; Mims, W. B.; Solomon, E. I. *J. Am. Chem. Soc.* **1989**, *111*, 6106−6123.
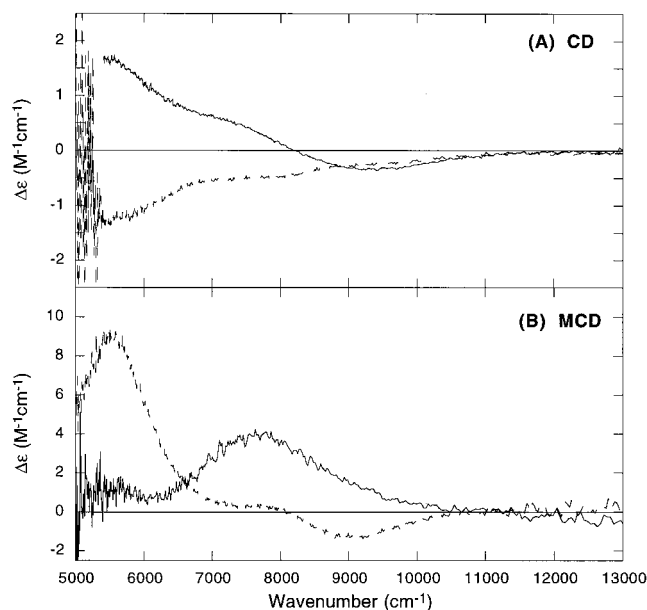

Figure 12. Orientation of the redox active orbitals of dioxygen and the active site of (A) reduced Δ^9-desaturase and (B) stearoyl-ACP Δ^9-desaturase. The axes used are the same as shown in Figure 3A,B.

would be that dioxygen has to bind to both irons for effective two-electron transfer to the two half-occupied antibonding π orbitals of dioxygen to give a peroxide level intermediate. Figure 12A shows the ligand-field estimate (Figure 3A,B) of the orientation of the redox active orbital, d_{yz}, for both irons. Dioxygen binding to the first iron would involve a π acceptor interaction with the d_{yz} orbital. However, the orientation of this orbital on the second iron would not allow reasonable overlap with the other half-occupied antibonding π^* orbital of dioxygen. This provides a possible explanation for the slow dioxygen reactivity of reduced Δ^9D. This model is currently being investigated using density functional calculations.

Substrate binding strongly perturbs the active site. The first iron remains 5-coordinate but is distorted toward a trigonal bipyramidal structure with a negative ZFS, D_1. The second iron changes to 4-coordinate with a positive ZFS, D_2. These results show that the ligand fields of the iron centers of reduced Δ^9D are greatly altered upon binding stearoyl-ACP. The two irons remain antiferromagnetically coupled, but the exchange coupling increases from $-J = <\sim1.0$ cm^{-1} to $-J = <\sim2.5$ cm^{-1}. This magnitude is still within the range observed for two μ-1,3 carboxylate bridges. This antiferromagnetic coupling generates an $M_s = \pm1$ ground state and an $M_s = \pm2$ plus two $M_s = 0$ excited states at ~2, ~9, and ~9 cm^{-1}, respectively. The low-lying $M_s = \pm2$ doublet splits in energy in the presence of a magnetic field, leading to a sublevel crossover and a change in the ground state. Thus, stearoyl-ACP perturbs both the ground and excited states when it binds to the active site of reduced Δ^9D. This interaction dramatically changes the geometric and electronic structure of the active site, resulting in an additional open coordination position on one iron, and significantly enhances the oxygen reactivity of the active site.

On the basis of the crystal structure of reduced ribonucleotide reductase (RR),[15] this dramatic change in the geometric structure of reduced Δ^9D upon substrate binding could be associated with

Figure 13. (A) CD and (B) LT MCD spectra of the reduced binuclear non-heme Fe(II)Fe(II) active site of ribonucleotide reductase (—) (adapted from ref 70) and stearoyl-ACP Δ^9-desaturase (- - -). The CD and low-temperature MCD spectra were recorded at 5 °C and 5 K, 7 T, respectively.

one of the terminal bidentate glutamic acid residues in the reduced active site becoming monodentate to generate a 4-coordinate iron center. This change would make the active site structure of stearoyl-ACP Δ^9-desaturase more similar to that of reduced RR, which has high dioxygen reactivity. Crystallographic results have shown that the active site of reduced RR has two 4-coordinate irons bridged by two μ-1,3 carboxylate bridges.[69] However, the terminal glutamic acid residue (Glu204) is fairly distorted. CD/MCD studies show that the active site of reduced RR has one 4-coordinate iron and one 5-coordinate iron.[70] Figure 13 compares the CD and MCD spectra of reduced RR (solid line) and stearoyl-ACP Δ^9D (dashed line). In RR, the 5-coordinate iron has been correlated with the high-energy band ($\sim$9300 cm^{-1}), and the 4-coordinate iron could contribute the two low-energy bands ($\sim$5500 cm^{-1}, $\sim$7000 cm^{-1}). The VTVH MCD and spin-Hamiltonian analysis showed that the two irons have opposite signs of ZFS with $D_1 = \sim-10$ cm^{-1} and $D_2 = \sim+5$ cm^{-1}, and an exchange coupling $-J$ of $\sim$0.5 cm^{-1}. These results are all very similar to those of stearoyl-ACP Δ^9D. Thus, while the active sites of reduced Δ^9D and RR are quite different, substrate binding to reduced Δ^9D causes a structural change, making the site more similar to reduced RR.

While reduced RR and stearoyl-ACP Δ^9D have similar ligand-field transition energies, ZFS, and exchange coupling, there are some differences in the sign and magnitude of their CD/MCD intensities. The relative intensities of the transitions observed in the CD spectra for both species are fairly similar (Figure 13A). The difference in sign between the transitions likely results from a conformational difference between the two active sites associated with substrate binding in reduced Δ^9D as observed with MMO.[45,71] In the MCD spectra (Figure 13B) the relative intensity of the two low-energy transitions reverses. A ligand-field calculation using the coordinates of the 4-coordinate site in reduced RR shows that this iron has a flattened tetragonal (D_{2d}) distortion. This D_{2d} distortion gives a d$_{z^2}$ ground state with the two transitions at $\sim$5500 and $\sim$7000 cm^{-1} (Figure 13, solid lines) assigned as the d$_{z^2} \rightarrow$ d$_{xz}$ and d$_{z^2} \rightarrow$ d$_{x^2-y^2}$ transitions, respectively. It is likely that the 4-coordinate iron

from stearoyl-ACP Δ^9D has a C_{3v} distortion due to the long N$_{His}$–Fe bond observed in the reduced crystal structure. In an elongated C_{3v} distortion, d$_{z^2}$ remains as the ground state, while the two low-energy transitions (Figure 13, dashed lines) would be the d$_{z^2} \rightarrow$ d$_{yz}$ and d$_{z^2} \rightarrow$ d$_{xz}$ transitions. Thus, two different distortions of a 4-coordinate iron site might be expected for reduced RR and stearoyl-ACP Δ^9D which have the same ZFS and LF transition energies but different selection rules. A ligand-field calculation of reduced Δ^9D with one of the bidentate terminal glutamic acid residues shifted to monodentate has also been performed. The results show a C_{3v} distorted tetrahedral structure with transitions at $\sim$5800 and $\sim$7800 cm^{-1}, which is within the range of those observed for stearoyl-ACP Δ^9D (Figure 5).

It should be emphasized that while reduced RR rapidly reacts with dioxygen, reduced Δ^9D is stable under dioxygen for hours. Alternatively, stearoyl-ACP Δ^9D rapidly reacts with dioxygen under multiple turnover conditions to yield oleyl-ACP. Figure 12B shows the approximate orientations of the redox active orbitals in the active site of stearoyl-ACP Δ^9D estimated from the above LF calculation. Compared to the poor orbital overlap of a bridging dioxygen anticipated from ligand-field calculations for reduced Δ^9D (Figure 12A), the 4-coordinate iron(II) center of stearoyl-ACP Δ^9D would have a d$_{z^2}$ ground state. This can provide a good σ interaction with one π^* orbital of dioxygen while the second π^* orbital can also have π overlap with the d$_{yz}$ orbital on the second iron. Hence, substrate binding could enhance the dioxygen reactivity through ligand-field changes that control orbital overlap. This possibility would be further pursued through electronic structure calculations.

In summary, the spectroscopic methodology applied in this study has provided detailed insight into the binuclear iron active site of reduced Δ^9D that has been correlated to the crystal structure. The geometric and electronic structures of reduced and substrate-bound Δ^9D have been evaluated. CD and MCD studies have shown that the reduced enzyme has two 5-coordinate irons with two-in–two-out distorted weak-axial square pyramidal geometries. The two irons are weakly antiferromagnetically coupled through μ-1,3 carboxylate bridges. Substrate binding dramatically changes the active site, with one of the irons becoming 4-coordinate, but still weakly antiferromagnetically coupled. The addition of substrate alters the active site of reduced Δ^9D toward a structure more similar to reduced RR, which significantly enhances its dioxygen reactivity. This substrate binding effect is similar to the component B effect observed for methane monooxygenase (MMO), for which MCD changes are also observed with component B binding.[45,71] These results suggest that the structures of the reduced biferrous enzymes alone are not necessarily those which correlate with dioxygen reactivity, and reveal that in Δ^9D substrate binding plays an important role in promoting the conversion of dioxygen to reactive catalytic intermediates. This substrate-induced control is not necessary for RR since the substrate of the reaction of the biferrous center with dioxygen is a Tyr residue already contained within the active site. However, the overall similarity of the MCD properties of reduced RR and stearoyl-ACP Δ^9D suggests that similar reactive intermediates will be observed, which may include the participation of a 4-coordinate iron site in the early phase of the dioxygen reaction.

Supporting Information Available: Correlation diagrams of the energy levels and energy splittings of the binuclear ferrous ground state including noncollinearity between the two iron atoms for reduced and substrate-bound Δ^9-desaturase, and simulations using the complete spin Hamiltonian in eq 1 for saturation-magnetization behavior of the MCD signal for reduced and substrate-bound Δ^9-desaturase (PDF). This material is available free of charge via the Internet at http://pubs.acs.org.